technologies

Article

Features of Metalorganic Chemical Vapor Deposition Selective Area Epitaxy of $Al_zGa_{1-z}As$ ($0 \leq z \leq 0.3$) Layers in Arrays of Ultrawide Windows

Viktor Shamakhov [1,*], Sergey Slipchenko [1,*], Dmitriy Nikolaev [1], Ilya Soshnikov [1,2,3], Alexander Smirnov [1], Ilya Eliseyev [1], Artyom Grishin [1], Matvei Kondratov [1], Artem Rizaev [1], Nikita Pikhtin [1] and Peter Kop'ev [1]

[1] Ioffe Institute, 26 Politekhnicheskaya, 194021 St. Petersburg, Russia; dim@mail.ioffe.ru (D.N.); ipsosh@mail.ru (I.S.); alex.smirnov@mail.ioffe.ru (A.S.); ilya.eliseyev@mail.ioffe.ru (I.E.); ar.evg.grishin@yandex.ru (A.G.); mikondratov99@gmail.com (M.K.); rizartem@mail.ioffe.ru (A.R.); nike@mail.ioffe.ru (N.P.); ps@kopjev.ioffe.ru (P.K.)
[2] Nanotechnology Center, Epitaxial Nanotechnology Laboratory at Alferov University, 194021 St. Petersburg, Russia
[3] Institute for Analytical Instrumentation, 31-33 Ivana Chernykh, 190103 St. Petersburg, Russia
* Correspondence: shamakhov@mail.ioffe.ru (V.S.); serghpl@mail.ioffe.ru (S.S.)

Abstract: $Al_zGa_{1-z}As$ layers of various compositions were grown using metalorganic chemical vapor deposition on a GaAs substrate with a pattern of alternating SiO_2 mask/window stripes, each 100 μm wide. Microphotoluminescence maps and thickness profiles of $Al_zGa_{1-z}As$ layers that demonstrated the distribution of the growth rate and z in the window were experimentally studied. It was shown that the layer growth rate and the AlAs mole fraction increased continuously from the center to the edge of the window. It was experimentally shown that for a fixed growth time of 10 min, as z increased from 0 to 0.3, the layer thickness difference between the center of the window and the edge increased from 700 Å to 1100 Å, and the maximum change in z between the center of the window and the edge reached Δz 0.016, respectively. Within the framework of the vapor -phase diffusion model, simulations of the spatial distribution of the layer thickness and z across the window were carried out. It was shown that the simulation results were in good agreement with the experimental results for the effective diffusion length D/k: Ga—85 μm, Al—50 μm.

Keywords: selective area epitaxy; mocvd; AlGaAs; photoluminescence; profilometry

Citation: Shamakhov, V.; Slipchenko, S.; Nikolaev, D.; Soshnikov, I.; Smirnov, A.; Eliseyev, I.; Grishin, A.; Kondratov, M.; Rizaev, A.; Pikhtin, N.; et al. Features of Metalorganic Chemical Vapor Deposition Selective Area Epitaxy of $Al_zGa_{1-z}As$ ($0 \leq z \leq 0.3$) Layers in Arrays of Ultrawide Windows. *Technologies* **2023**, *11*, 89. https://doi.org/10.3390/technologies11040089

Academic Editors: Sergey N. Grigoriev, Marina A. Volosova and Anna A. Okunkova

Received: 23 May 2023
Revised: 27 June 2023
Accepted: 29 June 2023
Published: 7 July 2023

1. Introduction

To date, one of the topical tasks in the field of photonic integrated circuits technology is the monolithic integration of electro-optical elements [1–6] that perform various functions, including the control and generation of both optical radiation (multiwave laser sources, modulators, low-loss waveguides, splitters, combiners, etc.) and electrical signals. One of the ways to effectively address this challenge is the selective area epitaxy (SAE) technique [7–10]. The main feature of this growth method is that epitaxial growth occurs on a pre-prepared substrate with a passivating mask deposited on the surface. This mask forms regions which suppress growth, while epitaxial growth occurs in unprotected regions (windows). At present, single-mode lasers with monolithically integrated modulators [11] and couplers [12], multiwavelength single-mode laser systems [13], monolithic semiconductor sources of femtosecond laser pulses [14], and tunable semiconductor lasers with ultra-wide tuning ranges [15] are fabricated using SAE. The state-of-the-art formation of nano-objects such as quantum dots [16] and nanowires [17] is also implemented using SAE. To date, the main SAE techniques are metalorganic chemical vapor deposition (MOCVD) [10,12], molecular beam epitaxy (MBE) [18], and chemical beam epitaxy (CBE) [19].

One of the characteristic features of SAE is associated with the influence of the geometric dimensions of the mask and windows on the composition and properties of the

grown epitaxial layers [20,21]. The fundamental reason for this behavior is related to mass conservation during the growth process. As a result, the reduction in the growth area associated with growth inhibition in the mask region leads to an increase in the growth rate in the window. In the SAE process, precursors can reach either the mask or the window [9] through migration inside the boundary layer of the gas phase. Precursors that reach the window region undergo a pyrolysis reaction and participate in the growth of the epitaxial layer. Precursors reaching the mask can either be adsorbed onto the mask surface and migrate to the window area through surface diffusion, or they can be desorbed from the mask surface within a short time. The desorbed precursors then return to the gas phase and diffuse towards the window due to the resulting concentration gradient between the mask and the window. The growth process is determined by the total contribution of these two diffusion processes. In addition, the diffusion in the gas phase is the dominant process in MOCVD according to references [22,23]. This is due to the fact that the diffusion length in the gas phase is much larger than the surface diffusion length. According to references [24,25], the diffusion length in the gas phase can reach up to 100 μm, while the surface diffusion length remains below 1 μm. As a result, the growth rate of the epitaxial layer increases, and its distribution becomes inhomogeneous within the window region.

It follows from the above discussion that the ability to predict the properties of deposited materials is important for SAE. To date, the most widely used model for MOCVD is the vapor-phase diffusion model [9,10,20,25,26]. In this model, the mask surface diffusion is neglected. Surface migration plays an important role only when the mask geometry is close to the surface diffusion length. This model has demonstrated its effectiveness, as it gives good agreement between the simulated and experimental results for binary layers [27].

However, there are no data in the literature on how the simulation results agree if several different values are taken for z. There are also almost no data for periodic structures in which neighboring elements are located (close enough) such that they can influence each other. An element refers to two stripes of the mask and the window between them. Isolated elements are typically studied, i.e., the neighboring element is most often located at a distance of more than 300 μm from the studied element.

The novelty of the results is in the fact that, for the first time, experimental and theoretical studies have been carried out on the growth of layers of AlGaAs/GaAs solid solutions obtained using the selective area epitaxy technique in ultrawide windows. The results are important to the development of selective area epitaxy techniques for the multilayer heterostructure growth used in many optoelectronic devices. Section 1 of this paper describes the features of the technology used for obtaining bulk layers of solid solutions of various compositions (composition of $Al_zGa_{1-z}As$ ($0 \leq z \leq 0.3$)) grown using selective area epitaxy on a GaAs substrate with a periodic structure consisting of alternating 100 μm wide stripes with and without SiO_2. In Section 2, the vapor-phase diffusion model is considered, which describes the selective area epitaxy of $Al_zGa_{1-z}As$ layers in ultrawide windows. Section 3 presents the results of experimental studies on the spatial distribution of the thickness and composition of the selective area epitaxy-grown $Al_zGa_{1-z}As$ layers, as well as the simulation results. Within the framework of the vapor-phase diffusion model, the effective diffusion lengths for Ga and Al were chosen to ensure good agreement between the simulation and experiment on thickness and composition variation across the window.

2. Materials and Methods

2.1. Fabrication of Experimental Samples

An EMCORE GS3100 (EMCORE Corp., Somerset, NJ, USA) setup with a vertical reactor and resistive heating of the substrate holder was used for epitaxial growth. The work pressure in the reactor was maintained about 77 Torr. The substrate temperature and rotation speed were 750 °C and 1000 rpm, respectively. Trimethylgallium (TMGa) and trimethylaluminum (TMAl) (Elma-Chem, Zelenograd, Russia) were used as sources of group 3 atoms, and arsine (AsH_3) (Salyut, Nizhny Novgorod, Russia) was used as the

source of group 5 atoms. The carrier gas was hydrogen (H_2). In this study, the growth time was fixed at 10 min for all samples. Two types of samples were fabricated. Both types of samples were grown on a precisely oriented n-GaAs (100) substrate 2 inches in diameter (Wafer Technology Ltd., Milton Keynes, UK). For the first type of samples (SE—standard epitaxy), standard epitaxial growth was carried out on a substrate without a mask. Four $Al_{z0}Ga_{1-z0}As$ samples were grown with the following compositions (z_0) and growth rates (V_{planar}): sample SE1—$z_0 = 0$, V_{planar} = 200 Å/min; sample SE2—$z_0 = 0.11$, V_{planar} = 225 Å/min; sample SE3—$z_0 = 0.19$, V_{planar} = 247 Å/min; sample SE4—$z_0 = 0.3$, V_{planar} = 286 Å/min. Samples of the second type were SAE-grown. To do this, at the initial stage, a pattern of alternating stripes (100 μm wide dielectric mask/100 μm wide window without a dielectric) oriented in the direction [011] was made on the substrate. The 1000 Å thick SiO_2 mask was deposited by ion-plasma sputtering. The pattern was formed using lithography and an etching process in a buffered oxide solution (BOE 5:1). Before the AlGaAs layer growth, the substrate with a pattern was annealed at a temperature of 750 °C for 20 min in the arsine flow, followed by the SAE process. As a result, four samples of the second type were grown with different z_0 at the same fluxes as for standard epitaxy: $z_0 = 0$ for SAE1; $z_0 = 0.11$ for SAE2; $z_0 = 0.19$ for SAE3; $z_0 = 0.3$ for SAE4. The actual compositions of the layers and their distribution in the window for all samples of the second type will be discussed below. It should be noted that the deposition of polycrystals on the mask was observed for the SAE4 sample under the given growth conditions (Figure 1a), but their density was not high, so the sample was not excluded from the studies. Figure 1a shows a segment located in the center of the mask. As can be seen from Figure 1a, for this area (12 × 9 μm), the number of polycrystals is about 400 pieces, which is an average density of about 3.7 pcs/μm^2. In this case, the linear dimensions of polycrystals do not exceed 100 nm. It should be noted that the density of polycrystals slightly decreases towards the mask/window interface. Also, one can observe a negligible number of polycrystals in the mask region within 1 μm from the mask/window interface. This behavior can be explained based on the study in [28]. For each type of reactant species, there is a certain threshold concentration on the mask surface, above which a heterogeneous nucleation occurs. This threshold is higher for ideal than for non-ideal areas of the mask surface (for example, roughness or defects on the mask surface). Polycrystals precipitate when one of the threshold concentrations is exceeded. Moreover, there is a region at the mask/window interface where nucleation does not occur. For comparison, Figure 1b shows an image of the mask surface for the SAE3 sample on which there are no polycrystals.

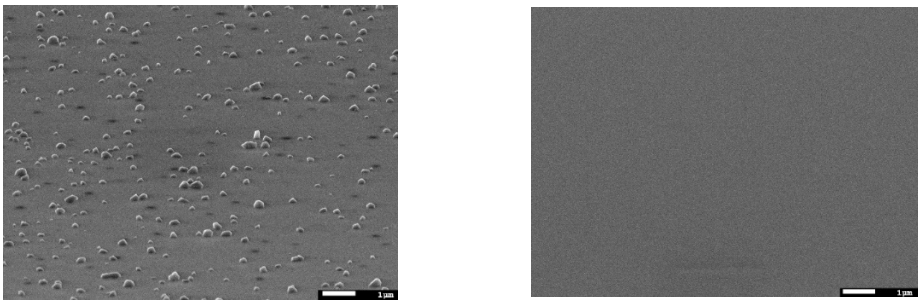

(**a**) (**b**)

Figure 1. Scanning electron microscope (SEM) JOEL JSM-7001F (JOEL Ltd., Tokyo, Japan) image of the surface in the center of the mask for SAE4 (**a**) and SAE3 (**b**) samples.

Further, the microphotoluminescence (μPL) spectra for samples of the second type (SAE2–SAE4) were studied with a spatial resolution in the window region. The μPL measurements were performed at room temperature (300 K) using a Horiba LabRAM HR Evolution UV-VIS-NIR (Horiba Jobin Yvon, Longjumeau, France) spectrometer equipped with a confocal microscope. The spectra were measured using the continuous-wave (cw) excitation at 532 nm (2.33 eV) of a Nd:YAG laser (Torus, Laser Quantum, Stockport, UK) with

a power on the samples as low as ~40 μW. The spectra were recorded using a 600 lines/mm grating and Peltier-cooled electron-multiplying charge-coupled device (EMCCD) detector, while a Leica PL FLUOTAR 50 × NIR (NA = 0.55) long working-distance objective lens was used to focus the incident beam onto a spot of ~2 μm diameter. The measurements were carried out with point-to-point scanning with a step of 1 μm. The *z*-distribution was determined for the selectively grown epitaxial layer from the obtained data. As an alternative to the proposed technique for determining the composition, energy-dispersive X-ray spectroscopy (EDS) can be used [29,30]. However, we consider it more labor-intensive and less accurate in resolution for spatial scanning.

Then, the mask was removed from the samples (SAE1–SAE4) using a buffer etchant. After that, the thickness distribution of the selectively grown epitaxial layer was measured across the window stripe for each sample. An AmBios XP-1 (Ambios Technology Inc., Santa Cruz, CA, USA) surface profilometer was used for the study.

2.2. SAE Simulation Model

The selective epitaxy process was quantitatively described using the vapor-phase diffusion model [9,10,20,25,26]. The simulation model is based on the calculation of the concentration profile of precursors in the gas phase above the substrate surface. The profile was determined by solving the Laplace equation in the boundary layer window of width F and height M. Figure 2 shows a schematic explaining the boundary conditions for the selective epitaxy process simulation within the vapor-phase diffusion model. In our case, we used a 2D model, because the length of the mask stripes was much greater than its width, which allowed us to neglect diffusion along the mask stripes. Then, the Laplace equation took the form:

$$\frac{\partial^2 N}{\partial x^2} + \frac{\partial^2 N}{\partial y^2} = 0, \quad (1)$$

where N is the precursor concentration, x is the coordinate in the direction across the window, and y is the coordinate in the direction perpendicular to the growth plane.

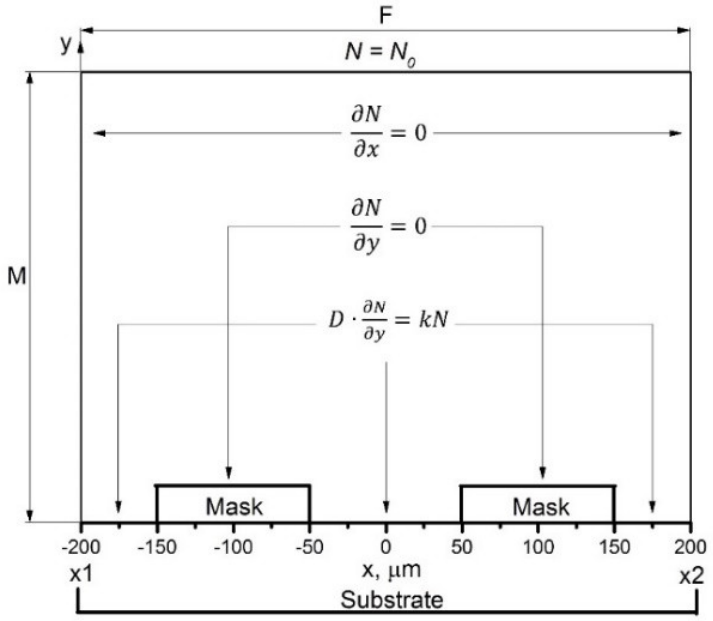

Figure 2. Two-dimensional simulation domain of the vapor-phase diffusion model. *F* and *M* are the width and height of the boundary layer. $x1$ and $x2$ are the boundaries of the simulation that takes place along the x axis.

The boundary conditions at the edges of the window and the boundary layer can be written as follows:

1—the upper part of the boundary layer is at a sufficiently large distance from the substrate to avoid perturbations introduced by the mask.

$$N|_{y=M} = N_0, \tag{2}$$

where N_0 is the precursor concentration at the upper boundary of the boundary layer, which is constant.

2—precursor concentration does not change in lateral directions within the boundary layer.

$$\frac{\partial N}{\partial x}|_{x=x1,x2} = 0 \tag{3}$$

3—precursors are not deposited on the surface of the mask.

$$\frac{\partial N}{\partial y}|_{y=0} = 0, \tag{4}$$

4—precursors are deposited on the surface of the semiconductor.

$$D \cdot \frac{\partial N}{\partial y}|_{y=0} = kN, \tag{5}$$

where k is a surface reaction rate constant; D is a mass diffusion constant.

The precursor concentration profile was determined by the D/k ratio, which can be considered as the effective diffusion length. D/k can be estimated either by theoretical calculation [9,26] or by fitting to experimental data.

To estimate the layer thickness distribution across the window, the concept of growth-rate enhancement (*GRE*) was used. *GRE* characterizes the layer growth-rate change during selective epitaxy relative to the growth rate during standard epitaxy, i.e., deposition on a substrate without a mask. *GRE* is calculated by:

$$GRE = \frac{H}{H_{planar}} = \frac{V}{V_{planar}} = \frac{N}{N_0} \cdot \left(1 + \frac{M}{\frac{D}{k}}\right), \tag{6}$$

where H and H_{planar} are the thicknesses of the selectively grown layer and the standard-grown layer, respectively; V and V_{planar} are the growth rates of the selectively grown layer and the standard-grown layer, respectively. It is worth noting here that the values of H_{planar} and V_{planar} are constant in the growth plane for standard epitaxy with the selected regimes, while there is a dependence on the x coordinate characterizing the lateral position in the window in the case of selective epitaxy.

These calculations are applicable for binary compounds. For ternary solid solutions of the $A_zB_{1-z}C$ type (where A and B are elements of the 3rd group), *GRE* is determined using a linear relationship between the binary compounds *AC* and *BC* forming a ternary solid solution [10]:

$$GRE_{ABC} = z_0 \cdot GRE_{AC} + (1 - z_0) \cdot GRE_{BC}, \tag{7}$$

where GRE_{ABC}, GRE_{AC}, and GRE_{BC} are *GREs* for the *ABC* solid solution and the binary compounds that form it, respectively; z_0 is the *AC* mole fraction under the same growth conditions at standard epitaxy.

According to [10], the z distribution of the $A_zB_{1-z}C$ solid solution across the window at SAE is determined by the GRE_{ABC} distribution and the composition z_0 of the $A_{z0}B_{1-z0}C$ solid solution at standard epitaxy according to the relation:

$$z = \frac{z_0 \cdot GRE_{AC}}{GRE_{ABC}}, \tag{8}$$

3. Results and Discussion

3.1. Studies of the SAE-Grown AlGaAs Layers' Thickness Profiles across the Window

We examined the SE samples to control the layer composition and the deposition rate prior to studying the SAE samples. To test the growth rate, SE1–SE4 samples were diced at their centers to obtain chips for scanning electron microscope (SEM) studies. Then, the thicknesses of the deposited layers were determined using SEM images. From the data obtained, the growth rate was determined, which coincided with the preset one with good accuracy. The PL spectra were also measured for these samples, from which the z_0 was determined, which corresponded to the specified composition with a high accuracy.

In the first part of the analysis of experimental results, let us consider the thickness profiles and determine the change in the thickness of the AlGaAs epitaxial layers across the window for samples SAE1–SAE4. For each sample, four neighboring windows were scanned. Figure 3 shows the measurement results (solid lines), and it is clear that with an increase in the AlAs mole fraction in the deposited AlGaAs layer (from SAE1 to SAE4), its thickness increases. It can be seen there is a fairly good reproducibility of the layer thicknesses in the windows for each sample. For the SAE1 sample, the thickness in the window center has values in the range of 3730–3860 Å, and at the window edge, 4430–4600 Å; for the SAE2 sample, it is of 4030–4080 Å in the center and 4820–4900 Å at the edge; for the SAE3 sample: 4270–4390 Å in the center and 5150–5400 Å at the edge; for the SAE4 sample: 4980–5150 Å in the center and 6090–6250 Å at the edge. It can be seen that the difference in the thickness of the selectively grown layer in the window center with respect to the edge increases with an increase in the AlAs mole fraction.

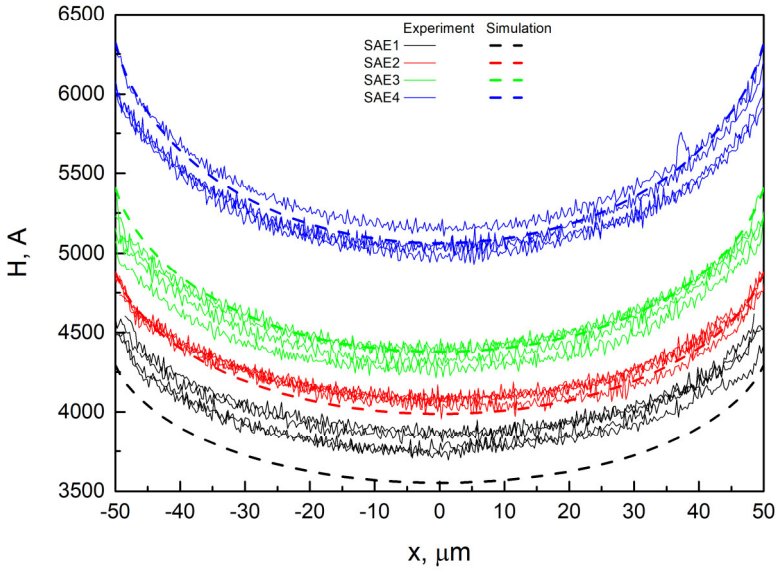

Figure 3. Profiles of the layer thickness across the window for SAE1–SAE4 samples. Solid lines are experimental data; dotted lines are simulation results.

Next, in order to compare the simulation model with the experimental results, the change in the layer thickness across the window during SAE for different z_0 corresponding to the SAE1–SAE4 samples was calculated. First, we chose the *D*/*k* for Ga, which provides the best agreement between the calculated thickness and the experimentally measured thickness for the SAE1 sample (GaAs layer) in the window center. GRE values were calculated for *D*/*k* ranging from 70 to 150 μm. In the simulation, the boundary layer height M was 1500 μm. Figure 4a shows the calculated GREs; it is clear that the GRE increases as *D*/*k* increases to 85 μm at the window center. A further increase in *D*/*k* leads to a decrease in GRE in the window center. For different values of *D*/*k* (μm), the GRE values (center/window edge) are as follows: 70 μm—1.775/2.219; 85 μm—1.776/2.146; 95 μm—1.775/2.107; 100 μm—1.774/2.09; 110 μm—1.771/2.058; 150 μm—1.752/1.963.

Also for the SAE1 sample, which has an experimental difference in layer thickness between the center and edge of the window of 700–740 A, the theoretical differences for various *D/k* values are as follows: 70 µm—888 Å; 85 µm—740 Å; 95 µm—664 Å; 100 µm—632 Å; 110 µm—574 Å; 150 µm—422 Å. The cumulative evidence is that the results closest to the experiment were obtained at *D/k* for Ga equal to 85 µm. For Al, we could not choose the *D/k* based on experimental data because of the active growth of the AlAs layer on the surface of the mask at SAE. In [21], the value of *D/k* for Ga coincides with the value chosen in the present study (85 µm); therefore, the *D/k* for Al of 50 µm also indicated in [21] was used in the simulation of SAE2–SAE4 samples. Figure 4b shows the GRE change over the window width for GaAs and AlAs binary compounds, as well as the AlGaAs GRE calculated using Equation (7) for the compositions z_0 corresponding to the SAE2–SAE4 samples. The resulting GRE values for the center/edge of the window are 1.776/2.146, 1.775/2.17, 1.774/2.188, and 1.772/2.212 for SAE1, SAE2, SAE3, and SAE4, respectively. It can be seen that the GRE difference between the center and the edge increases with increasing AlAs mole fraction.

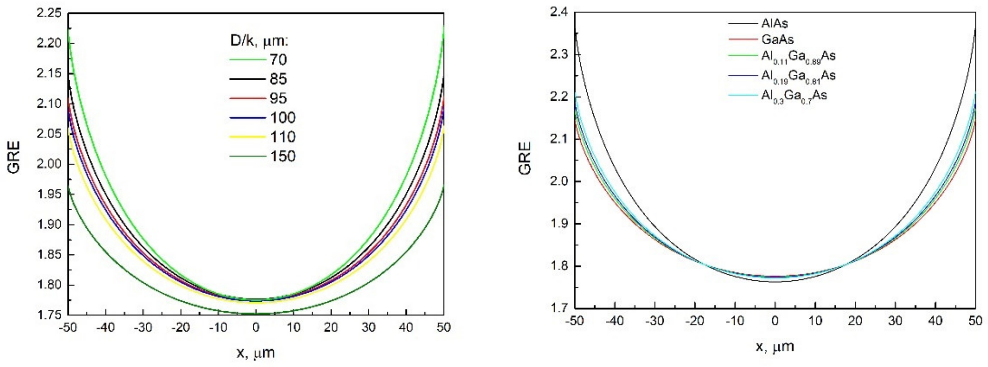

(**a**) (**b**)

Figure 4. Simulated GRE distribution across the window: (**a**) for *D/k* ranging from 70 to 150 µm; (**b**) for AlAs and GaAs binary compounds, as well as for $Al_{z0}Ga_{1-z0}As$ solid solutions with z_0 (at standard epitaxy) of 0.11, 0.19, and 0.3, obtained at *D/k* ratios of 85 µm and 50 µm for Ga and Al, respectively.

Figure 4b shows that a decrease in the *D/k* ratio leads to an increase in the GRE difference between the edge and the center of the window. A lower *D/k* ratio indicates that the precursors are adsorbed onto the substrate at a higher rate. Consequently, most of the precursors were deposited in the window near the window/mask interface, and the *GRE* decreased more rapidly with distance from the window/mask interface. As a result, the AlGaAs solid solutions turned out to be enriched in Al near the window/mask interface.

The layer thickness distribution across the window was calculated for samples SAE1–SAE4 using the obtained *GRE* profiles (Figure 4b). The layer thickness was calculated based on Equation (6):

$$H = GRE \cdot H_{planar} = GRE \cdot V_{planar} \cdot t, \quad (9)$$

where t is the layer growth time.

Figure 3 (dashed curves) shows the calculated layer thickness distribution across the window for SAE1–SAE4 samples and it is seen that the calculated curves are in good agreement with the experimental data. The change in the layer thickness in the center and at the edge of the window (experiment/simulation) was also compared, which was: 700–740/740 Å, 790–820/890 Å, 880–1010/1020 Å, and 1100–1110/1250 Å for SAE1, SAE2, SAE3, and SAE4 samples, respectively. It can be seen that the experimental difference in the layer thickness between the center and the edge of the window is in good agreement with that of the simulation. From the obtained results, we can conclude that the simulation is

in good agreement with the experimental results for the composition range $0 \leq z_0 \leq 0.3$ of $Al_{z0}Ga_{1-z0}As$ solid solutions at *D/k* ratios of 85 μm and 50 μm for Ga and Al, respectively.

3.2. Studies of the SAE-Grown AlGaAs Layers' Composition Profiles across the Window

In the second part of the experimental results analysis, let us compare the simulated and experimental profiles across the window of SAE-grown AlGaAs layers with different values of *z*. To this end, the μPL spectra were measured for SAE2–SAE4 samples at 300 K with a scanning step of 1 μm across the window. Figure 5 shows μPL spectra maps for SAE2–SAE4 samples. For all samples, a blue shift is observed when moving from the center to the edge of the window. For SAE2 (Figure 5a), a local peak of low intensity is observed in the 820–880 nm wavelength range, which was caused by the emission of the n-GaAs substrate. It can also be noted that the intensity of the PL spectrum increases towards the edge of the window relative to the center in the SAE2 and SAE3 samples, which coincides with the behavior of the PL spectrum measured by our group for AlGaAs at a temperature of 80 K in [26]. The SAE4 sample shows the opposite behavior compared with the SAE2 and SAE3 samples, i.e., the intensity of the PL spectrum at the edge of the window is lower than that at the center of the window. However, the reason for this behavior is not yet clear.

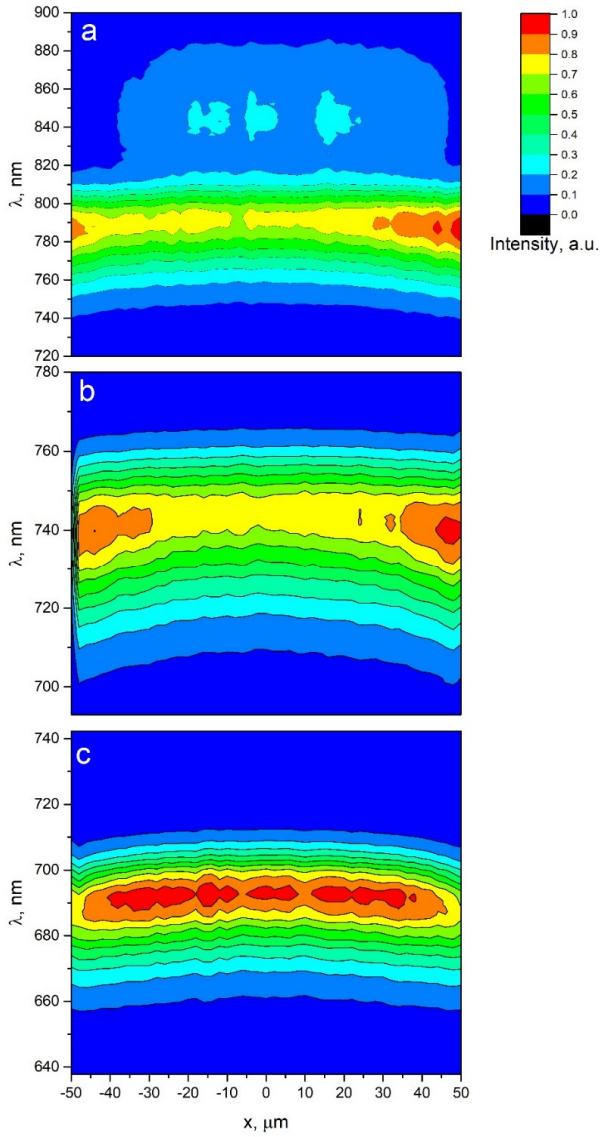

Figure 5. Maps of the μPL spectra measured at 300 K showing the spatial distribution of the spectral position and intensity of the PL spectra for the samples: (**a**)—SAE2, (**b**)—SAE3, (**c**)—SAE4.

From the μPL spectra obtained, z profiles across the window were plotted for the SAE2–SAE4 samples. To calculate z of the $Al_zGa_{1-z}As$ solid solution, the following relation between the band gap E and z was used [31]:

$$E = 1.424 + 1.247 \cdot z \ (z \leq 0.45) \quad (10)$$

Figure 6 (solid curves) shows z profiles across the window calculated using μPL spectra and Equation (10) for SAE2–SAE4 samples. Figure 6 (dashed lines) shows z profiles calculated using Equation (8) based on the vapor-phase diffusion model. Figure 6 shows that the simulation and experiment are in good agreement in the middle of the window for the SAE2 and SAE3 samples, and as the distance from the center to the edge of the window increases, the experimental values of z become slightly higher than the calculated ones. The experimental curve for the SAE4 sample is below the calculated one, which may be due to the formation of a small amount of polycrystals on the mask. Polycrystals can contain Al mainly, which leads to a decrease in the amount of Al diffusing towards the window in the gas phase. The change in z between the center and edge of the window for SAE-grown $Al_zGa_{1-z}As$ layers (experiment/simulation) was: 0.111/0.109 and 0.124/0.12, 0.191/0.189 and 0.205/0.206, and 0.293/0.298 and 0.309/0.321 in the center and at the edge of the window for the SAE2, SAE3, and SAE4 samples, respectively. We can conclude that the simulation model allows us to estimate the change in z across the window for $Al_zGa_{1-z}As$ solid solutions up to z = 0.3 with good accuracy. It should be noted that the experimental z variation between the center and edge of the window ranges from 0.013 to 0.016 as z_0 increases from 0.11 to 0.3, and the simulation gives an increase in this variation from 0.011 to 0.023.

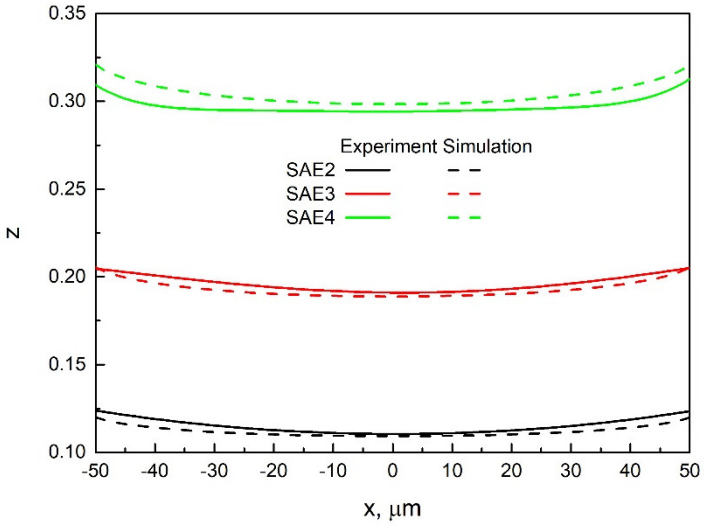

Figure 6. Profiles of the composition of $Al_zGa_{1-z}As$ layers across the window for samples SAE2–SAE4. Solid curves were obtained from the experimental data on μPL; dotted curves were simulated based on the vapor-phase diffusion model.

4. Conclusions

The behavior of the spatial variation of the main characteristics of $Al_zGa_{1-z}As$ epitaxial layers ($0 \leq z \leq 0.3$) grown via selective area epitaxy in arrays of ultra-wide windows (the growth rate, the layer thickness, and the layer composition distribution) have been determined on the basis of experimental studies of their properties. Comparison of experimental results with simulation in the framework of the vapor-phase diffusion model demonstrates a satisfactory agreement at D/k ratios of 85 μm and 50 μm for Ga and Al, respectively, which implies that the proposed simulation model is suitable for predicting the properties of layers in the development of multilayer structures and devices based on

them. In the future, the results obtained will be used in the study of strained quantum wells, which is crucial in the field of light-emitting structures.

Author Contributions: Conceptualization, V.S. and S.S.; methodology, V.S. and S.S.; formal analysis, V.S.; investigation, D.N., I.S., A.S. and I.E.; writing—original draft preparation, V.S. and S.S.; writing—review and editing, V.S. and S.S.; visualization, A.G., M.K. and A.R.; supervision, N.P. and P.K.; project administration, N.P.; funding acquisition, N.P. All authors have read and agreed to the published version of the manuscript.

Funding: This research received no external funding.

Institutional Review Board Statement: Not applicable.

Informed Consent Statement: Not applicable.

Data Availability Statement: All the data taken in this work have been published in this paper.

Acknowledgments: The authors would like to thank Ilya Shashkin for his assistance in the preparation of the manuscript.

Conflicts of Interest: The authors declare no conflict of interest.

References

1. Williams, K.A.; Bente, E.A.J.M.; Heiss, D.; Jiao, Y.; Ławniczuk, K.; Leijtens, X.J.M.; van der Tol, J.J.G.M.; Smit, M.K. InP photonic circuits using generic integration [Invited]. *Photon. Res.* **2015**, *3*, B60–B68. [CrossRef]
2. Zhang, C.; Li, X. III–V Nanowire Transistors for Low-Power Logic Applications: A Review and Outlook. *IEEE Trans. Electron. Devices* **2016**, *63*, 223–234. [CrossRef]
3. Dietrich, C.P.; Fiore, A.; Thompson, M.G.; Kamp, M.; Höfling, S. GaAs integrated quantum photonics: Towards compact and multi: Functional quantum photonic integrated circuits. *Laser Photonics Rev.* **2016**, *10*, 870–894. [CrossRef]
4. Zhang, C.; Miao, X.; Chabak, K.D.; Li, X. A review of III–V planar nanowire arrays: Selective lateral VLS epitaxy and 3D transistors. *J. Phys. D Appl. Phys.* **2017**, *50*, 393001. [CrossRef]
5. Bogdanov, S.; Shalaginov, M.Y.; Boltasseva, A.; Shalaev, V.M. Material platforms for integrated quantum photonics. *Opt. Mater. Express.* **2017**, *7*, 111–132. [CrossRef]
6. Smit, M.; Williams, K.; van der Tol, J. Past, present, and future of InP-based photonic integration. *APL Photonics* **2019**, *4*, 050901. [CrossRef]
7. Heinecke, H.; Milde, A.; Baur, B.; Matz, R. Selective-area growth of III/V semiconductors in chemical beam epitaxy. *Semicond. Sci. Technol.* **1993**, *8*, 1023–1031. [CrossRef]
8. Coleman, J.J. Metalorganic chemical vapor deposition for optoelectronic devices. *Proc. IEEE* **1997**, *85*, 1715–1729. [CrossRef]
9. Kim, J.D.; Chen, X.; Coleman, J.J. 10 Selective Area Masked Growth (Nano to Micro). In *Handbook of Crystal Growth*, 2nd ed.; Kuech, T.F., Ed.; Elsevier: Amsterdam, The Netherlands, 2015; Volume 3A, pp. 441–481. [CrossRef]
10. Wang, B.; Zeng, Y.; Song, Y.; Wang, Y.; Liang, L.; Qin, L.; Zhang, J.; Jia, P.; Lei, Y.; Qiu, C.; et al. Principles of Selective Area Epitaxy and Applications in III–V Semiconductor Lasers Using MOCVD: A Review. *Crystals* **2022**, *12*, 1011. [CrossRef]
11. Delprat, D.; Ramdane, A.; Silvestre, L.; Ougazzaden, A.; Delorme, F.; Slempkes, S. 20-Gb/s integrated DBR laser-EA modulator by selective area growth for 1.55-μm WDM applications. *IEEE Photon. Technol. Lett.* **1997**, *9*, 898–900. [CrossRef]
12. Osowski, M.L.; Lammert, R.M.; Coleman, J.J. A dual-wavelength source with monolithically integrated electroabsorption modulators and Y-junction coupler by selective-area MOCVD. *IEEE Photon. Technol. Lett.* **1997**, *9*, 158–160. [CrossRef]
13. Fujii, T.; Takeda, K.; Nishi, H.; Diamantopoulos, N.-P.; Sato, T.; Kakitsuka, T.; Tsuchizawa, T.; Matsuoand, S. Multiwavelength membrane laser array using selective area growth on directly bonded InP on SiO2/Si. *Optica* **2020**, *7*, 838–846. [CrossRef]
14. Xu, J.; Liang, S.; Liu, S.; Qiao, L.; Sun, S.; Deng, Q.; Zhu, H. Passively mode-locked quantum-well laser with a saturable absorber having gradually varied bandgap. *IEEE Photon. Technol. Lett.* **2017**, *29*, 889–892. [CrossRef]
15. Lemaıtre, F.; Latkowski, S.; Fortin, C.; Lagay, N.; Pajkovic, R.; Smalbrugge, E.; Decobert, J.; Ambrosius, H.; Williams, K. Selective area growth in generic integration for extended range tunable laser source. In Proceedings of the 2018 IEEE Photonics Conference (IPC), Reston, VA, USA, 30 September–4 October 2018; pp. 1–2. [CrossRef]
16. Kim, H.; Wei, W.; Kuech, T.F.; Gopalan, P.; Mawst, L.J. Room temperature operation of InAs quantum dot lasers formed by diblock-copolymer lithography and selective area MOCVD growth. In Proceedings of the 2017 IEEE Photonics Conference (IPC), Orlando, FL, USA, 1–5 October 2017; pp. 405–406. [CrossRef]
17. Barrigón, E.; Heurlin, M.; Bi, Z.; Monemar, B.; Samuelson, L. Synthesis and applications of III–V nanowires. *Chem. Rev.* **2019**, *119*, 9170–9220. [CrossRef]
18. Nishinaga, T.; Bacchin, G. Selective area MBE of GaAs, AlAs and their alloys by periodic supply epitaxy. *Thin Solid Films* **2000**, *367*, 6–12. [CrossRef]
19. Zannier, V.; Li, A.; Rossi, F.; Yadav, S.; Petersson, K.; Sorba, L. Selective-Area Epitaxy of InGaAsP Buffer Multilayer for In-Plane InAs Nanowire Integration. *Materials* **2022**, *15*, 2543. [CrossRef]

20. Gibbon, M.; Stagg, J.P.; Cureton, C.G.; Thrush, E.J.; Jones, C.J.; Mallard, R.E.; Pritchard, R.E.; Collis, N.; Chew, A. Selective-area low-pressure MOCVD of GaInAsP and related materials on planar InP substrates. *Semicond. Sci. Technol.* **1993**, *8*, 998–1010. [CrossRef]
21. Decobert, J.; Dupuis, N.; Lagreeb, P.Y.; Lagay, N.; Ramdane, A.; Ougazzaden, A.; Poingt, F.; Cuisin, C.; Kazmierski, C. Modeling and characterization of AlGaInAs and related materials using selective area growth by metal-organic vapor-phase epitaxy. *J. Cryst. Growth* **2007**, *298*, 28–31. [CrossRef]
22. Colas, E.; Shahar, A.; Soole, B.D.; Tomlinson, W.J.; Hayes, J.R.; Caneau, C.; Bhat, R. Lateral and longitudinal patterning of semiconductor structures by crystal growth on nonplanar and dielectric-masked GaAs substrates: Application to thickness-modulated waveguide structures. *J. Cryst. Growth* **1991**, *107*, 226–230. [CrossRef]
23. Kayser, O. Selective growth of InP/GaInAs in LP-MOVPE and MOMBE/CBE. *J. Cryst. Growth* **1991**, *107*, 989–998. [CrossRef]
24. Yamaguchi, K.-I.; Okamoto, K. Lateral Supply Mechanisms in Selective Metalorganic Chemical Vapor Deposition. *Jpn. J. Appl. Phys.* **1993**, *32*, 1523–1527. [CrossRef]
25. Sugiyama, M. Selective area growth of III-V semiconductors: From fundamental aspects to device structures. In Proceedings of the 22nd International Conference on Indium Phosphide and Related Materials (IPRM), Kagawa, Japan, 31 May–4 June 2010; pp. 1–6. [CrossRef]
26. Shamakhov, V.; Nikolaev, D.; Slipchenko, S.; Fomin, E.; Smirnov, A.; Eliseyev, I.; Pikhtin, N.; Kop'ev, P. Surface Nanostructuring during Selective Area Epitaxy of Heterostructures with InGaAs QWs in the Ultra-Wide Window. *Nanomaterials* **2021**, *11*, 11. [CrossRef] [PubMed]
27. Slipchenko, S.; Shamakhov, V.; Nikolaev, D.; Fomin, E.; Soshnikov, I.; Bondarev, A.; Mitrofanov, M.; Pikhtin, N.; Kop'ev, P. Basics of surface reconstruction during selective area metalorganic chemical vapour-phase epitaxy of GaAs films in the stripe-type ultra-wide window. *Appl. Surf. Sci.* **2022**, *588*, 152991. [CrossRef]
28. Yamaguchi, K.-I.; Okamoto, K. Analysis of Deposition Selectivity in Selective Epitaxy of GaAs by Metalorganic Chemical Vapor Deposition. *Jpn. J. Appl. Phys.* **1990**, *29*, 2351–2357. [CrossRef]
29. Eraky, M.S.; Sanad, M.M.S.; El-Sayed, E.M.; Shenouda, A.Y.; El-Sherefy, E.-S. Phase transformation and photoelectrochemical characterization of Cu/Bi and Cu/Sb based selenide alloys as promising photoactive electrodes. *AIP Adv.* **2019**, *9*, 115115. [CrossRef]
30. Eraky, M.S.; Sanad, M.M.S.; El-Sayed, E.M.; Shenouda, A.Y.; El-Sherefy, E.-S. Influence of the electrochemical processing parameters on the photocurrent–voltage conversion characteristics of copper bismuth selenide photoactive films. *Eur. Phys. J. Plus* **2022**, *137*, 907. [CrossRef]
31. Casey, H.C.; Panish, M.B. *Heterostructure Lasers Part B: Materials and Operating Characteristics*; Academic Press: San Francisco, CA, USA; London, UK, 1978; 344p.